Cell Reports

Report

SLC7A11 protects amoeboid-disseminating cancer cells from oxidative stress

Graphical abstract

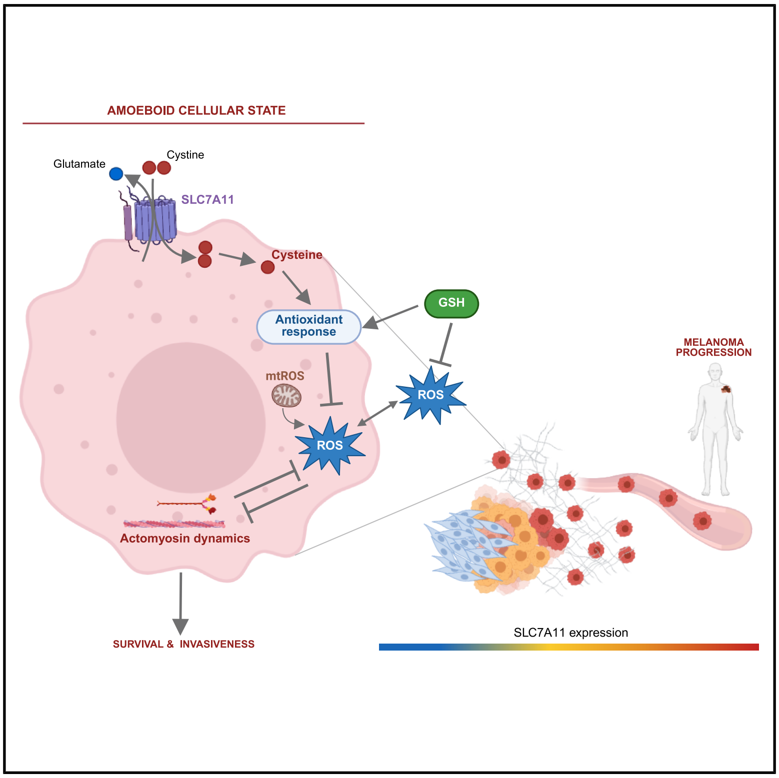

Authors

Vittoria Graziani, Jaume Barcelo, Aurelien Tripp, ..., George Poulogiannis, Eva Crosas-Molist, Victoria Sanz-Moreno

Correspondence

eva.crosas-molist@icr.ac.uk (E.C.-M.),
victoria.sanz-moreno@icr.ac.uk (V.S.-M.)

In brief

Graziani et al. show that SLC7A11 increases during melanoma disease progression. SLC7A11 promotes Myosin II-driven amoeboid invasive behavior while shielding amoeboid cancer cells from oxidative stress. Blocking SLC7A11 function represents a potential strategy to prevent metastatic spread.

Highlights

- Cancer cells increase SLC7A11 levels at tumor invasive fronts and in metastatic lesions
- SLC7A11 supports high ROCK-Myosin II activity and low oxidative stress
- Targeting SLC7A11 reduces invasion and survival of amoeboid metastatic cancer cells

Graziani et al., 2025, Cell Reports *44*, 115939
July 22, 2025 © 2025 The Authors. Published by Elsevier Inc.
https://doi.org/10.1016/j.celrep.2025.115939

Cell Reports

CellPress
OPEN ACCESS

Report

SLC7A11 protects amoeboid-disseminating cancer cells from oxidative stress

Vittoria Graziani,[1,2] Jaume Barcelo,[1,2] Aurelien Tripp,[3] Dipanwita Das,[1] Oscar Maiques,[1,2]
Joshua Alexander James Martin,[1,2] Joanne Sewell,[2] Andrea Vinaga,[2] Manon Liautard,[2] Rosa M. Marti,[4]
Xavier Matias-Guiu,[5,6] George Poulogiannis,[3] Eva Crosas-Molist,[1,2,*] and Victoria Sanz-Moreno[1,2,7,*]
[1]Cytoskeleton and Cancer Metastasis Laboratory, The Breast Cancer Now Toby Robins Research Centre Division of Breast Cancer Research, The Institute of Cancer Research, Chester Beatty Laboratories, London SW3 6JB, UK
[2]Barts Cancer Institute, Queen Mary University of London, John Vane Science Building, Charterhouse Square, London EC1M 6BQ, UK
[3]Signalling and Cancer Metabolism Laboratory, Division of Cell and Molecular Biology, the Institute of Cancer Research, 237 Fulham Road, London SW3 6JB, UK
[4]Department of Dermatology, Hospital Universitari Arnau de Vilanova, University of Lleida, IRBLleida, CIBERONC, 25198 Lleida, Spain
[5]Department of Pathology and Molecular Genetics, Hospital Universitari Arnau de Vilanova, University of Lleida, IRBLleida, CIBERONC, 25198 Lleida, Spain
[6]Department of Pathology, Hospital Universitari de Bellvitge University of Barcelona, IDIBELL, CIBERONC, L'Hospitalet-Barcelona, 08907 Barcelona, Spain
[7]Lead contact
*Correspondence: eva.crosas-molist@icr.ac.uk (E.C.-M.), victoria.sanz-moreno@icr.ac.uk (V.S.-M.)
https://doi.org/10.1016/j.celrep.2025.115939

SUMMARY

Oxidative stress limits metastasis, and amoeboid cancer cells have been identified in a variety of cancers as a subset of metastatic cancer cells characterized by high Rho-ROCK-driven Myosin II activity. They display fast individual migration and have increased survival abilities during metastasis. Amoeboid migrating cells require lower mitochondrial metabolism, but how they maintain low oxidative stress remains unclear. Using a combination of cancer cell lines in complex matrices, mouse xenografts, patient databases, and tissue microarrays, we show that SLC7A11 is highly expressed in amoeboid cancer cells, at the invasive front of primary tumors, and in metastatic lesions. We find that high SLC7A11 expression supports cancer cell survival and 3D invasion by promoting Myosin II activity while protecting cancer cells against oxidative stress. Targeting SLC7A11 effectively impairs amoeboid behavior, highlighting its potential as a therapeutic vulnerability in metastatic melanomas.

INTRODUCTION

Metastasis is a key clinical challenge underscoring the need to identify critical targets in cancer dissemination. Key pivotal steps in the metastatic cascade involve deregulated cell migration[1] and increased cell survival under different metabolic stress conditions.[2] Ameboid cell migration is characterized by rapid movement and a rounded cell morphology.[3] This migratory mode relies on increased Myosin II activity, which leads to membrane blebs functioning as both protrusions and pro-survival platforms.[4–6] Rho A/C activate Rho-associated protein kinases (ROCK1 and ROCK2), which in turn phosphorylate Myosin Light Chain II (MLC2), enhancing Myosin II-driven actomyosin contractility.[7]

Amoeboid cancer cells are highly metastatic, therapy resistant, and immune suppressive, highlighting their ability to survive certain stresses.[6] The prevalence of amoeboid cells at the invasive front (IF) of tumors correlates with aggressiveness, poor prognosis, and resistance to therapy,[8,9] while these cells have been identified in a range of different cancer types, including melanoma,[7,8,10–12] breast,[13] liver,[14,15] pancreatic,[16] prostate,[17] and head and neck[18] cancer. Some aspects of their aggressive behavior can be eradicated with ROCK inhibitors (ROCKis),[19,20] which are currently in active development,[19] but treatments specifically targeting these aggressive cells are urgently needed.[4,19]

On the other hand, metabolic plasticity is crucial during metastatic dissemination.[21] Amoeboid cancer cell migration is supported by lower mitochondrial metabolism associated with overall lower levels of oxidative stress.[6,22] However, how amoeboid cells sustain low levels of intracellular reactive oxygen species (ROS) is not fully understood, although there are some connections to lower Rac GTP levels[14,23] and lower adhesion strength.[24] Cellular adaptations such as increased levels of ROS-detoxifying enzymes and reductive power are crucial for cancer cells to survive in high oxidative stress such as that encountered in circulation.[2] Glutathione (GSH), comprising cysteine, glutamate, and glycine, plays a crucial role in this process.[25] Cysteine availability, the rate-limiting step in GSH synthesis, is essential. Cancer cells often rely on importing cystine through the Xc^- antiporter system. This transporter is composed of two subunits: SLC3A2 (4F2hc), a heavy-chain glycoprotein, and SLC7A11 (xCT), the transport module. Although SLC3A2 plays a crucial role in

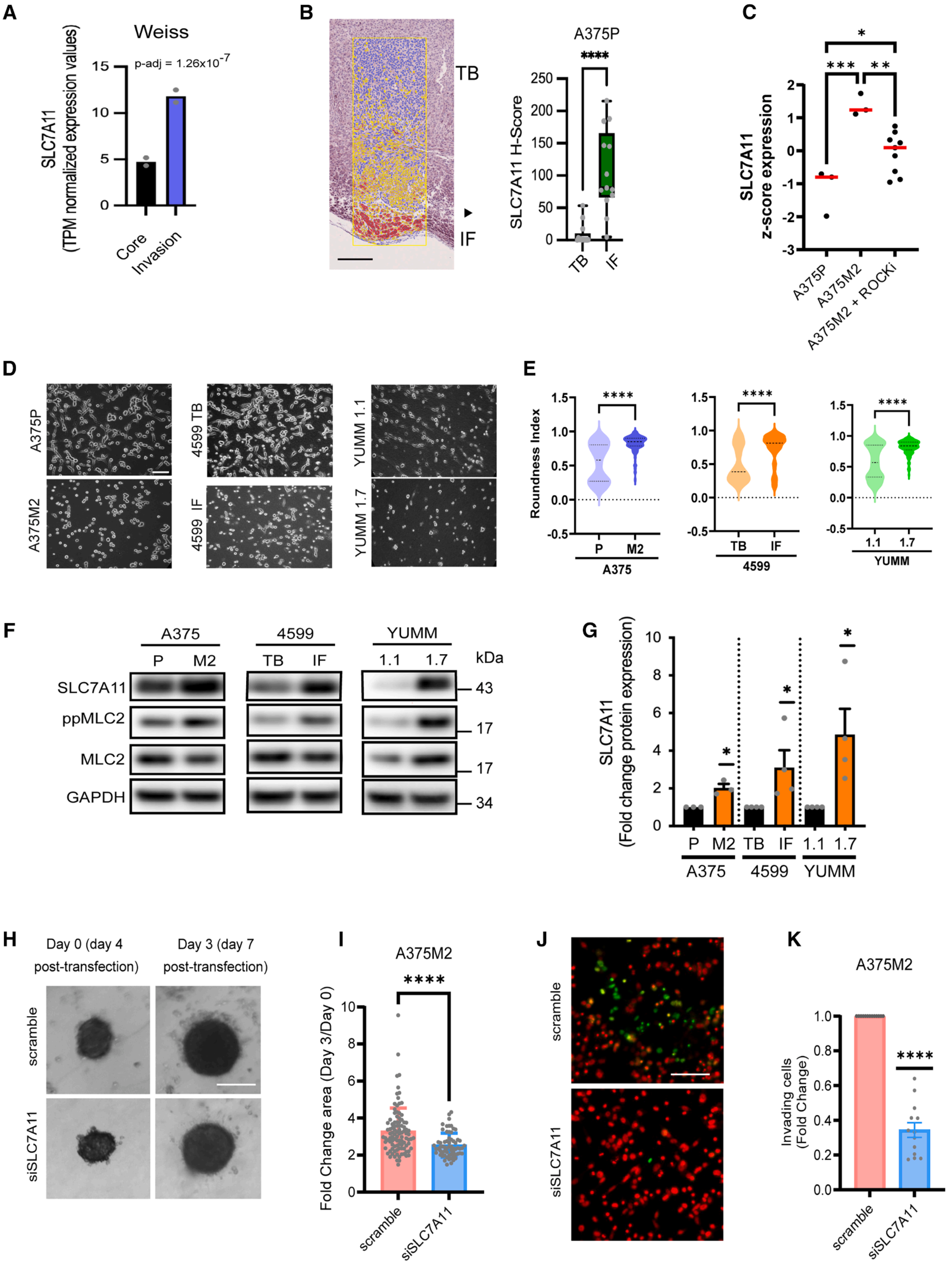

Figure 1. SLC7A11 expression is associated with amoeboid metastatic features

(A) RNA-seq data of SLC7A11 expression levels in invading cells compared to the non-migratory core from MV3 spheroids embedded in collagen I (GEO: GSE215750).

(B) Representative QuPath mark-up image and quantification of SLC7A11 in intradermal tumors in mice from A375P cells (*n* = 13 tumors/group). Scale bar, 200 μm.

(legend continued on next page)

guiding the transporter to the plasma membrane, its direct contribution to transport activity is less clearly defined compared to the active transport function of SLC7A11.[26] Inhibiting SLC7A11 disrupts GSH homeostasis and leads to an accumulation of ROS, ultimately causing cell death via ferroptosis.[27] Given the low ROS levels present in highly metastatic ameboid cancer cells,[6,14,22–24,28] we hypothesize that targeting their antioxidant capacity could impair their survival and invasive properties—both crucial for their metastatic potential.

RESULTS

SLC7A11 promotes amoeboid behavior

GSH—the main antioxidant in cells—is a tripeptide (γ-L-glutamyl-L-cysteinylglycine) using cysteine as a rate-limiting precursor.[29] SLC7A11 imports cystine—the oxidized form of cysteine—which is rapidly reduced in the cytosol and used for GSH synthesis, while glutamate is exported in exchange. By sustaining GSH levels, SLC7A11 supports redox balance and protects cancer cells from oxidative stress.[30] SLC7A11 is therefore frequently upregulated in various cancers, where its overexpression is associated with poor prognosis.[25,31,32]

Amoeboid cancer cells are predominant at the invasive front of primary tumors, and their presence in this site has been linked to an enhanced capability to invade surrounding tissues and eventually metastasize.[7,8,12,24] Due to its crucial role in redox homeostasis, we sought to investigate whether SLC7A11 promotes amoeboid behavior. We analyzed RNA sequencing (RNA-seq) data using MV3 melanoma cells cultured as spheroids embedded in collagen,[33] comparing cells from the core versus invading cells. The analysis revealed that SLC7A11 mRNA expression was more than 2-fold higher in invading cells than in cells from the core (Figure 1A).

To investigate this observation further, we employed isogenic melanoma cell lines. A375M2 cells are highly metastatic, predominantly rounded melanoma cells (∼90% rounded) characterized by elevated Myosin II activity.[34,35] These cells are derived from the less metastatic, more elongated A375P melanoma cells (50% rounded and 50% elongated) with lower Myosin II activity. This makes the A375P/A375M2 system a good model for studying amoeboid behavior.[34,35] A375P cells were orthotopically injected into the dermis of immunodeficient mice. Immunohistochemical analysis of the resulting tumors revealed elevated SLC7A11 protein expression at the IF compared to the tumor bodies (TBs) (Figure 1B).

Next, to investigate the link between actomyosin contractility and SLC7A11 expression, we analyzed mRNA data from an Affymetrix microarray by comparing A375M2 and A375P cells cultured on a collagen I matrix, as well as A375M2 cells treated with ROCK or Myosin II inhibitors.[7] This analysis revealed that SLC7A11 mRNA expression was positively associated with high actomyosin contractility: A375M2 cells showed higher levels of SLC7A11 gene expression than A375P cells or A375M2 cells treated with ROCKi or the direct Myosin inhibitor blebbistatin (Figure 1C). On the other hand, mRNA levels of SLC3A2, the other subunit of the system Xc^- antiporter, did not show this association (Figure S1A). SLC3A2 forms heterodimers with various other light-chain transporters[36] and may play more complex roles in disease progression.

To validate this result in other systems and at the protein level, we measured SLC7A11 protein in A375M2 versus A375P cells and two additional pairs of melanoma cell lines. 4599 cells were derived from murine melanomas harboring $Braf^{V600E}$.[37] We further grew 4599 cells as intradermal tumors in mice, and once the tumors were established, we isolated 4599 IF and 4599 TB cells from the IF and the TB. 4599 IF cells are more rounded (Figures 1D and 1E) and harbor higher activity of Myosin II than 4599 TB cells (Figures 1F and 1G). Lastly, YUMM1.1 (elongated with low Myosin II) and YUMM1.7 (rounded with high Myosin II and high amoeboid content) are derived from murine melanomas harboring $Braf^{V600E/wt}$ *Pten*$^{-/-}$ Cdkn2 (Figures 1D–1G).[38] In all isogenic pairs, cancer cells with high levels of active Myosin II and amoeboid content showed higher protein levels of SLC7A11 when compared with their counterparts with lower levels of Myosin II (Figures 1F and 1G).

To investigate the role of SLC7A11 in ameboid melanoma cells, we assessed the functional consequence of its depletion using invasive growth assays. Small interfering RNA (siRNA)-mediated knockdown of SLC7A11 in A375M2 cells significantly impaired their invasive growth potential (Figures 1H, 1I, S1B, and S1C). Moreover, SLC7A11 loss resulted in a reduced ability to invade through a 3D collagen matrix (Figures 1J and 1K). Importantly, the loss of cell rounding and decreased levels of phosphorylated MLC2 (ppMLC2) were observed after SLC7A11 depletion (Figures S1D–S1I).

Our findings show that SLC7A11 is consistently upregulated in multiple amoeboid cancer models. Moreover, SLC7A11 regulates amoeboid behavior, including cytoskeletal dynamics, 3D individual invasion, and 3D invasive growth.

(C) Expression levels of SLC7A11 from an Affymetrix microarray comparing highly contractile (A375M2) versus low contractile melanoma cells (A375P or A375M2 treated for 16 h with ROCK inhibitor (Y27632 [10 μM] or H1152 [5 μM]) or blebbistatin (2.5 μM) seeded on a thick layer of collagen I (GEO: GSE23764).

(D) Representative bright-field images. Scale bar, 500 μm.

(E) Quantification of cell morphology (>280 cells pooled from *n* = 3).

(F) Western blots for the indicated proteins and cell lines (A375 *n* = 3, 4599 *n* = 4, and YUMM *n* = 4).

(G) SLC7A11 western blot quantification normalized by GAPDH (A375 *n* = 3, 4599 *n* = 4, and YUMM *n* = 4).

(H) Representative bright-field images of A375M2 spheroids embedded in a collagen I matrix, comparing scramble control to SLC7A11 silencing on days 0 and 3 (*n* = 3). Scale bar, 100 μm.

(I) Quantification of invasive growth from (H), represented as fold change in area from day 3 to day 0 (*n* = 3).

(J) Representative images from a 3D invasion assay, showing invading cells in green and cells at the bottom of the matrix in red. Scale bar, 100 μm.

(K) Invasion assay quantification from (J), showing fold change of invasion in A375M2 scramble versus siSLC7A11 treatment (*n* = 4).

p values by one-way ANOVA with Tukey's correction (A), Mann-Whitney test (B), ordinary one-way ANOVA (C), unpaired t test (E and I), and one sample t test (G and K). For all graphs, $^*p < 0.05$, $^{**}p < 0.01$, and $^{***}p < 0.001$. See also Figure S1.

SLC7A11 is associated with melanoma invasiveness and metastatic progression

To assess the relevance of SLC7A11 in melanoma progression, we analyzed mRNA levels in published datasets, comparing melanoma cell lines to normal melanocytes (Philadelphia and Mannheim datasets). This analysis revealed an increase in SLC7A11 expression during melanoma progression (Figure 2A). Consistent with this finding, further evaluation of patient-derived gene expression data from Gene Expression Omnibus (GEO) datasets—Kabbarah, Talantov, and Riker—as well as The Cancer Genome Atlas (TCGA) showed that SLC7A11 expression is notably upregulated, particularly in metastatic lesions (Figure 2B). On the other hand, SLC3A2 did not show a consistent increase during metastatic progression (Figure S2A), suggesting that SLC7A11 levels better predict disease aggressiveness.

We next analyzed SLC7A11 protein levels in human melanoma tissue microarrays. SLC7A11 protein was upregulated in metastasis compared to matched primary tumors (Figure 2C). Importantly, comparing matched TBs and IFs from the same patients, we found higher protein levels of SLC7A11 at the IF in both primary tumors and metastatic lesions (Figures 2D and 2E). These data show that the upregulation of SLC7A11 mRNA and protein is an adaptation of melanoma cells that are progressing to metastatic stages.

One of the mechanisms through which SLC7A11 promotes tumor progression is through suppression of ferroptosis, often via facilitating glutathione peroxidase 4 (GPX4)-mediated detoxification of lipid peroxides.[27] We therefore analyzed GPX4 protein levels in our cellular models and found that in amoeboid melanoma cells, high SLC7A11 protein levels can be associated with either higher (in the 4599 and YUMM isogenic models) or lower GPX4 levels (in A375 isogenic model) (Figures S2B and S2C). Using TCGA data, we observed that high SLC7A11 expression in patients with melanoma could be associated with either high or low GPX4 levels (Figures S2D and S2E). Moreover, patients could be separated into two distinct subgroups depending on the expression of different ferroptosis-related genes (Figures S2D and S2E). These findings indicate that SLC7A11 could contribute to metastatic progression, and in certain patients, this effect may occur independently of GPX4 levels.

Extracellular GSH protects amoeboid cancer cells from oxidative stress

Our findings suggest that elevated SLC7A11 expression levels in amoeboid cancer cells may play a crucial role in counteracting oxidative stress encountered during metastatic dissemination.[2,39] Importantly, extracellular GSH mitigates oxidative stress within the tumor microenvironment, promoting disease progression.[40,41]

To directly evaluate whether protection from oxidative stress enhances Myosin II-driven amoeboid behavior, we treated A375P cells with GSH. This led to an increase in cell roundness while reducing the proportion of elongated cells (Figures 3A and 3B), an effect replicated in elongated 4599 and YUMM1.1 cells (Figures S3A and S3B). Conversely, inhibition of amoeboid behavior with a ROCKi (GSK269962A or H1152) in A375M2 cells was reversed by GSH supplementation (Figures S3C–S3H), suggesting that GSH supports amoeboid cytoskeletal features.

To further investigate the impact of oxidative stress in amoeboid cells in culture, we exposed cells to redox-disrupting agents, including menadione (vitamin K3), a synthetic naphthoquinone that increases ROS levels, and L-BSO, an inhibitor of γ-GCS that impairs GSH synthesis and ROS detoxification. Our results show that menadione treatment significantly reduced A375M2 cell viability compared to the vehicle control, an effect exacerbated by two SLC7A11 inhibitors,[42] erastin (1 μM) and sulfasalazine (SAS; 200 μM) (Figure 3C). Notably, GSH supplementation rescued cell viability in the presence of menadione, both alone and in combination with erastin or SAS. Furthermore, cotreatment with menadione and L-BSO resulted in a more pronounced reduction in cell viability compared to menadione treatment alone, an effect that was rescued by GSH supplementation (Figure 3D). Liquid chromatography-mass spectrometry (LC-MS) analysis confirmed that treatment with menadione and L-BSO decreased the ratio of reduced to oxidized glutathione (GSH/GSSG) (Figure 3E), supporting the induction of an oxidative cellular state.[43] Reduced GSH was derivatized with N-ethylmaleimide (NEM) to form Glutathione-S-ethylmaleimide (GS-NEM) and prevent GSH auto-oxidation. Accurate measurement of the GSH/GSSG ratio was measured as GS-NEM/GSSG ratio (Figure 3E). Additionally, a decrease in the intracellular NAD^+/NADH ratio was observed (Figure 3F), indicating redox imbalance and impaired energy metabolism.[44]

Previous studies have linked ROCK-Myosin II activity levels to redox balance.[23,24] As such, extracellular ROS can enter the cell and suppress actomyosin and ameboid features,[23] while the downregulation of ROCK activity results in Rac activation and increased total intracellular ROS levels.[23] Similar to menadione, treating A375M2 cells with ROCKis (H1152 and GSK269962A) or the Myosin II inhibitor blebbistatin increased mtROS levels in particular (Figures S3I and S3J), while GSH supplementation reversed mtROS and restored Myosin II activity levels (Figures S3E–S3H and S3J).

To investigate the role of GSH in the context of SLC7A11 depletion, we used LC-MS analysis. We first measured intracellular cysteine levels, the rate-limiting precursor for GSH synthesis,[30] and observed that SLC7A11 silencing led to a significant reduction in intracellular cysteine (Figure 3G). Similar to GSH, cysteine was measured as cysteine–NEM (Figure 3G). Notably, this decrease was rescued by extracellular GSH supplementation, suggesting that GSH can compensate to some extent for impaired cystine uptake (Figure 3G). This effect could also be due to the breakdown of GSH into its constituent amino acids, including cysteine.[45] Next, to determine whether extracellular GSH supplementation restores amoeboid invasive behavior through direct uptake or by buffering extracellular ROS levels that could enter the cell, we supplemented cells with $^{13}C_2$,^{15}N-labeled GSH and performed LC-MS analysis after 24 h. We detected incorporation of the labeled GSH into intracellular pools—approximately 10% of total intracellular GSH was the isotopolog m+3 GS-NEM—indicating that extracellular GSH is directly taken up by cells. Importantly, this uptake occurred independently of SLC7A11 expression, as the levels of labeled GSH were comparable between control and SLC7A11-silenced cells (Figure 3H). These findings suggest that GSH supplementation may influence ROS homeostasis both inside and outside cells. To further validate

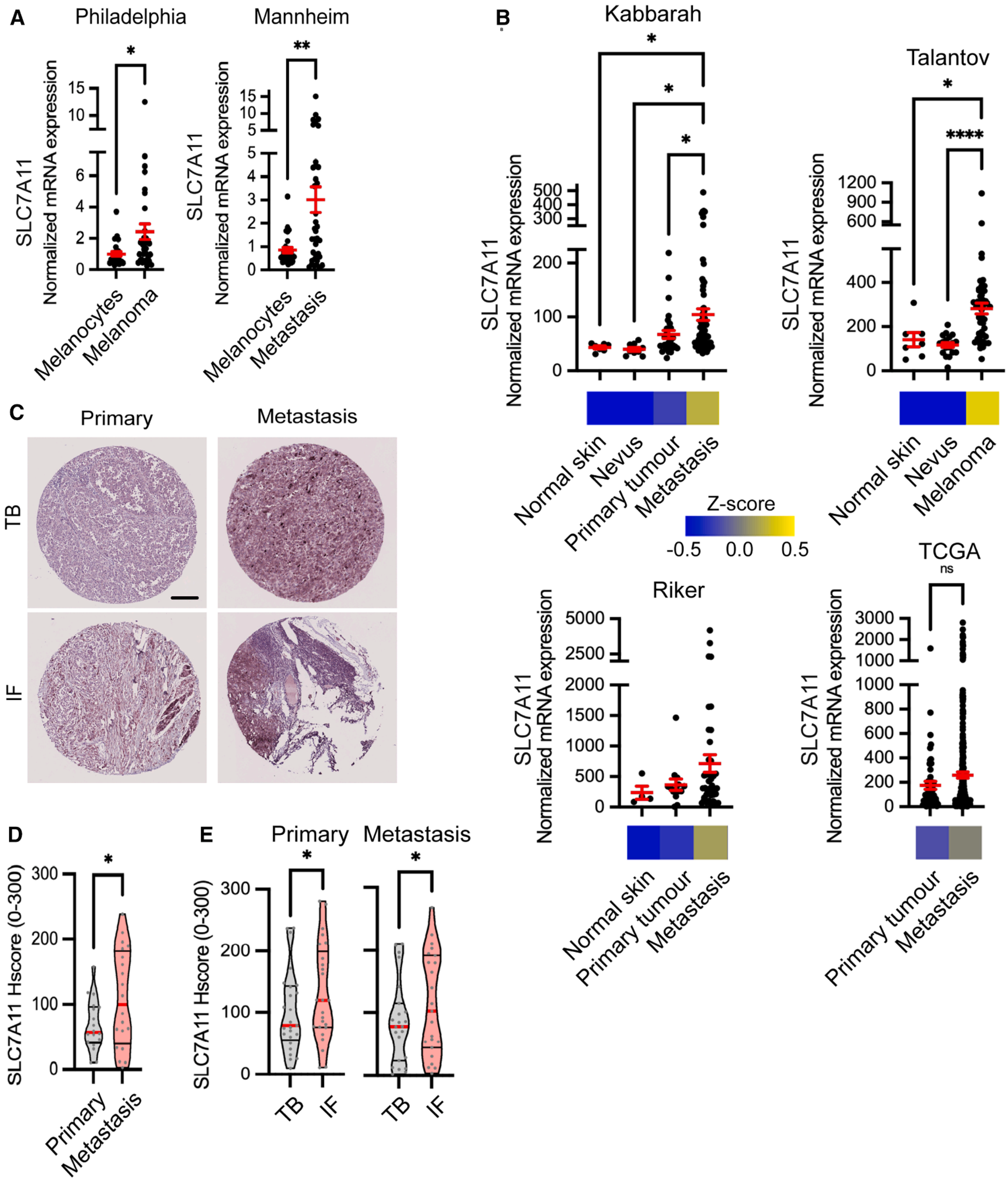

Figure 2. SLC7A11 expression correlates with melanoma invasiveness and progression

(A) Expression levels of SLC7A11 in melanoma cell lines compared to primary melanocytes from the indicated databases.

(B) Expression levels of SLC7A11 using data from GEO, Kabbarah (GEO: GDS1989), Talentov (GEO: GSE3189), Riker (GEO: GSE7553), and TGCA during melanoma progression.

(C) Representative immunohistochemistry (IHC) images for SLC7A11 in matched TBs and IFs of primary tumors and metastasis from human melanoma tissue microarrays. Scale bar, 200 μm.

(D) SLC7A11 IHC quantification from (C) comparing primary tumors and metastasis from human melanoma tissue microarrays ($n = 20$).

(E) SLC7A11 IHC quantification from (C) comparing matched TBs and IFs of primary tumors and metastasis ($n = 25$ matched primary tumors, $n = 23$ matched metastasis).

p values by one way ANOVA with Tukey's correction (B), unpaired t test (A and D), and paired t test (E). For all graphs, $^{*}p < 0.05$, $^{***}p < 0.001$, and $^{****}p < 0.0001$. See also Figure S2.

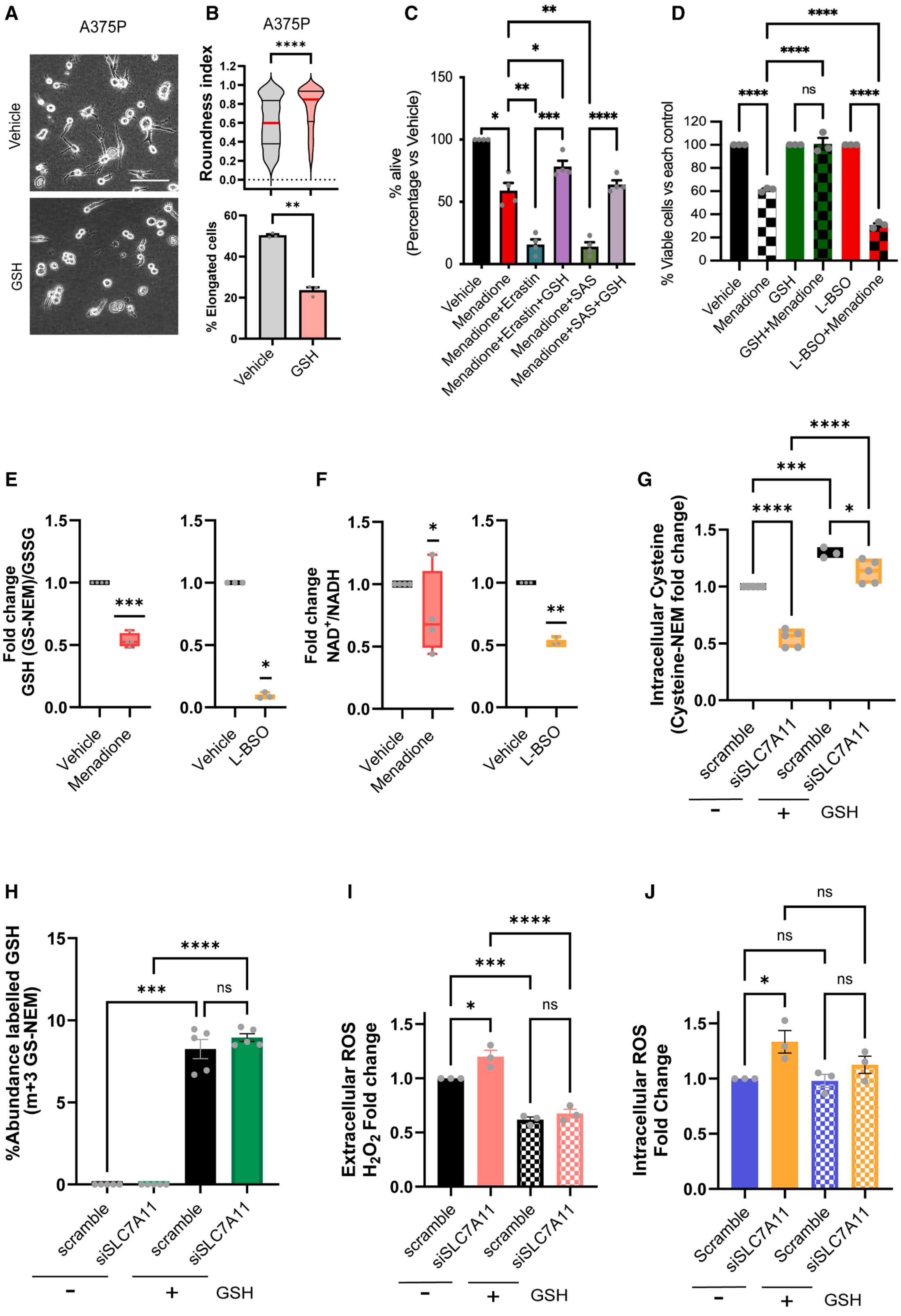

(legend on next page)

this, we measured both intracellular and extracellular ROS levels. Even under basal conditions, SLC7A11 downregulation—without additional oxidative stress—resulted in increased ROS levels both intracellularly and extracellularly. Notably, no ROS increase was detected after SLC7A11 knockdown if the cells had been supplemented with GSH—and this was true for both compartments (Figures 3I and 3J). These data show that GSH contributes to balancing ROS levels inside amoeboid cancer cells and in their microenvironment.

In conclusion, SLC7A11 plays a role in maintaining redox balance within the tumor microenvironment and sustaining amoeboid cancer cell behavior. Moreover, by buffering oxidative stress, GSH further supports amoeboid cytoskeletal features while promoting cell survival.

Amoeboid cancer cells are highly sensitive to SLC7A11 inhibition

To understand if SLC7A11 targeting could be a strategy to reduce amoeboid aggressive behaviors, we treated all isogenic cell pairs with erastin and found that amoeboid cancer cells (A375M2, 4599 IF, and YUMM1.7) exhibited higher sensitivity to this SLC7A11 inhibitor than their less metastatic counterparts (A375P, 4599 TB, and YUMM 1.1) (Figure 4A). Consistent with previous findings,[46] we observed that treatment with erastin (1 μM) induced cell death via ferroptosis in amoeboid cells, as this effect was completely rescued by co-treatment with ferrostatin-1 (1 μM) (Figure 4B), a specific ferroptosis inhibitor.[46]

Importantly, treatment with erastin (1 μM) led to a marked reduction in invasive growth, an effect that was fully rescued by GSH ectopic supplementation (Figures 4C and 4D). The rescue of the invasive properties of melanoma cells could be in part due to the ability of GSH to induce ameboid features (Figures 4E and 4F). Similar results were obtained using SAS (Figures 4G and 4H). Since both drugs can have off-target effects,[47,48] we confirmed our results using SLC7A11 depletion via RNAi (Figures S4A–S4D).

These data show that SLC7A11 is not only a hallmark but a vulnerability of amoeboid cancer cells, indicating its potential as a therapeutic target.

DISCUSSION

Amoeboid cancer cells have been identified at the edge of primary tumors[7,8,12,24] and are characterized by a unique cytoskeleton, high metastatic potential, immunosuppressive and drug-resistant capabilities,[6,22] and low levels of ROS.[23]

In the current work, we observed increased SLC7A11 protein levels in cells was located at the IF of tumors, where amoeboid cancer cells are located. Consistently, our data show that highly metastatic amoeboid cancer cells upregulate both SLC7A11 mRNA and protein compared to their less metastatic counterparts. Moreover, our findings reveal that SLC7A11 plays a critical role in supporting amoeboid cancer cell invasiveness by sustaining high Myosin II activity. We find that SLC7A11 levels are associated with melanoma progression in patients, suggesting its potential involvement in the metastatic process when disseminating cancer cells need to survive in oxidative environments such as the bloodstream.[2]

Interestingly, SLC7A11 expression levels in patients can be associated with either higher or lower GPX4 levels. Based on association with other ferroptosis-related genes, we can speculate that SLC7A11^{high} GPX4^{high} tumors could possibly rely on GPX4 to evade ferroptosis,[49] while SLC7A11^{high} GPX4^{low} tumors could activate alternative survival pathways, such as NRF2-driven signaling.[50] While ferroptosis induction holds promise for tumor eradication, systemic GPX4 inhibition poses a risk to both adaptive and innate immune functions.[51] In contrast, targeting SLC7A11 presents a potentially safer therapeutic approach, as it is not an essential gene.[51] SLC7A11 inhibitors are used to treat conditions such as ulcerative colitis and rheumatoid arthritis, demonstrating favorable bioavailability and safety profiles. Additionally, these inhibitors are currently being evaluated in clinical trials for solid tumors (ClinicalTrials.gov: NCT06134388, NCT03847311, NCT04205357, and NCT00528047).

Our findings suggest that extracellular GSH is important in maintaining redox homeostasis. Exposure to redox-disrupting agents or inhibition of SLC7A11 led to an accumulation of ROS, which was reversed by exogenous GSH supplementation. This protective effect could be in part due to GSH preventing ROS intracellular accumulation. Such high intracellular ROS could support the activity of ARHGAP5[23]—a Rho-GAP activated by ROS that downregulates Rho-ROCK-Myosin II activity in amoeboid melanoma cells.[52] Moreover, GSH could play a role in detoxifying ROS through S-glutathionylation—a post-translational modification involving cysteine residues on proteins.[53] Since actin is susceptible to S-glutathionylation, impacting actin polymerization and becoming dysregulated during oxidative stress,[54–57] we can speculate that GSH

Figure 3. GSH protects amoeboid cancer cells from oxidative stress

(A) Representative bright-field images of A375P cells seeded on a collagen I matrix and treated with 10 mM glutathione (GSH) for 24 h. Scale bar, 100 μm.

(B) Quantification of cell roundness in A375P cells ($n = 3$). The top image shows violin plots representing the median with interquartile range, and the bottom image shows mean ± SEM.

(C) Percentage of viable A375M2 cells after 48 h of treatment with menadione (10 μM), erastin (1 μM), GSH (10 mM), and/or SAS (250 μM) ($n = 3$).

(D) Percentage of viable A375M2 cells after 48 h of treatment with menadione (10 μM), GSH (10 mM), and/or L-BSO (250 μM) ($n = 3$).

(E) LC-MS quantification of GSH (GS-NEM)-to-GSSG ratio in A375M2 cells under the indicated conditions ($n = 5$).

(F) LC-MS quantification of NAD+/NADH ratio in A375M2 cells under the indicated conditions ($n = 5$).

(G) LC-MS quantification of cysteine, shown as cysteine-NEM fold change relative to the untreated scramble.

(H) LC-MS quantification of intracellular percentage abundance of labeled GSH (m+3 GS-NEM) in A375M2 cells under the indicated conditions.

(I) Extracellular ROS (H_20_2) measured with Amplex red kit (see STAR Methods).

(J) Intracellular ROS levels were measured by flow cytometry (see STAR Methods).

For all graphs, statistical analysis was performed using one-way ANOVA with Tukey's (C and D) or Šídák's correction (G–J), Mann-Whitney test (B, top), unpaired t test (B, bottom), and one-sample t test (E and F). Data are presented as mean ± SEM, with $^*p < 0.05$, $^{**}p < 0.01$, and $^{****}p < 0.0001$. See also Figure S3.

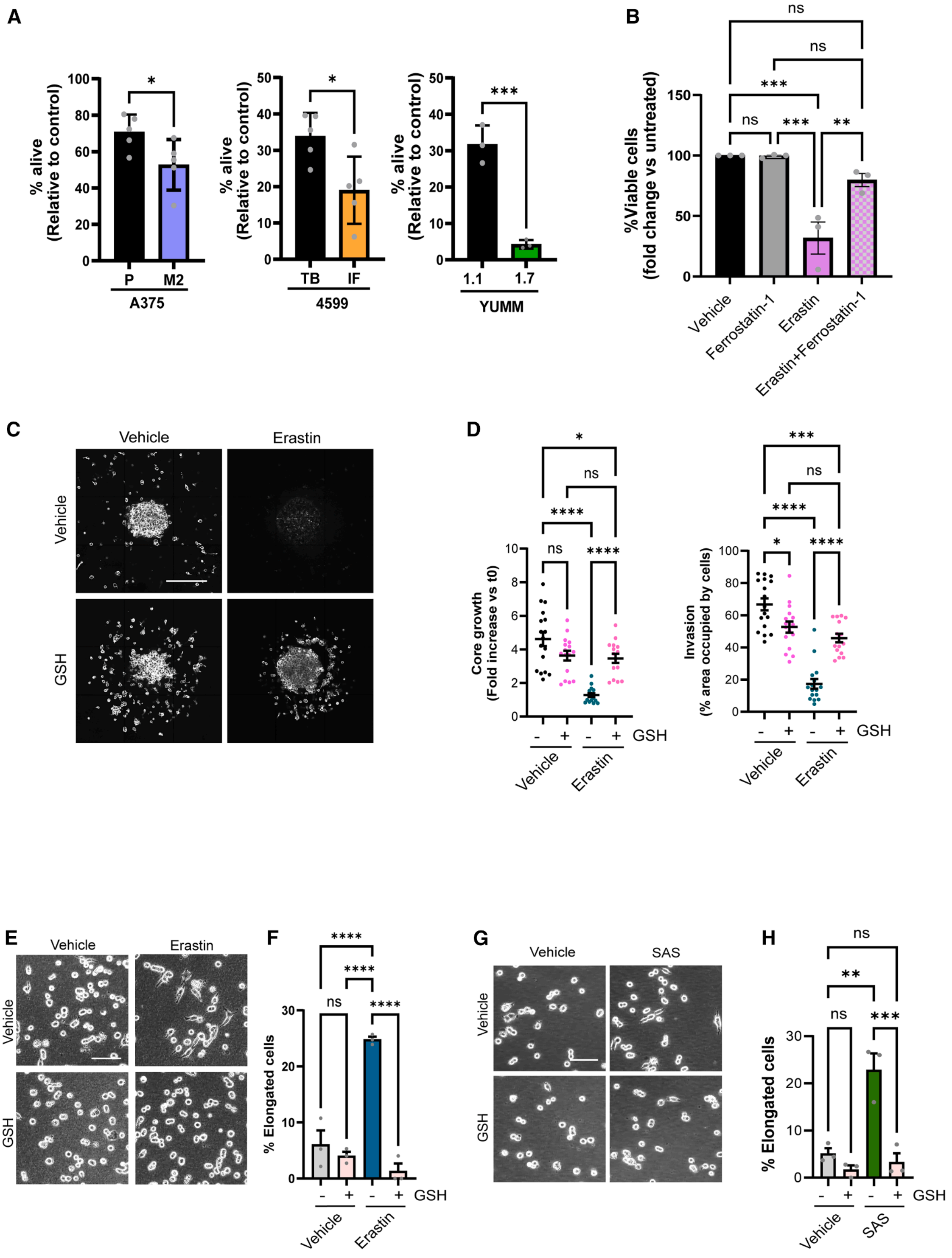

Figure 4. SLC7A11 inhibition leads to loss of amoeboid features

(A) Percentage of viable cells after 72 h of treatment with SLC7A11 inhibitor (1 μM erastin for A375 cells and 0.25 μM erastin for 4599 and YUMM cells) (*n* = 3). Data are presented as mean ± SEM (*n* = 4).

(B) Percentage of viable A375M2 cells after 48 h of treatment with erastin (1 μM) in the presence or absence of ferrostatin-1 (1 μM).

(C) Representative F-actin staining images of YUMM1.7 spheroids embedded in a collagen I matrix and treated with glutathione (GSH; 10 mM), SLC7A11 inhibitor (erastin, 1 μM), or both for 72 h (*n* = 3). Scale bar, 200 μm.

(D) Quantification of core growth (left) and invasion (right) from (B) (*n* = 3).

(legend continued on next page)

could further control cytoskeletal dynamics via actin S-glutathionylation.

Beyond redox balance, SLC7A11 plays a role in cellular processes such as protein synthesis and nutrient availability.[58] By exporting glutamate, SLC7A11 dampens glutamate- and glutamine-dependent processes, including mitochondrial respiration.[58] This aligns with our previous findings, where we demonstrated that amoeboid metastatic cancer cells exhibit lower levels of oxidative phosphorylation (OXPHOS) than their low metastatic counterparts.[24]

Overall, inhibiting SLC7A11 emerges as a promising therapeutic strategy to target amoeboid cancer cells and prevent or inhibit melanoma cell invasion and survival. Our analysis reveals that SLC7A11 increased mRNA and that protein synthesis is an adaptation of invasive and metastatic cancer cells. This suggests a potential therapeutic opportunity where patients with primary tumors characterized by high levels of SLC7A11 could benefit from anti-metastatic treatments targeting SLC7A11. Additionally, SLC7A11 could serve as a biomarker for amoeboid cells, aiding in patient stratification and the development of personalized treatments.

Limitations of the study

This study identifies SLC7A11 as a key regulator of redox balance and amoeboid behavior in metastatic melanoma. However, limitations should be considered. While SLC7A11 inhibitors showed efficacy, off-target effects have been described.[47,48] We addressed this by using both SMARTpool and ON-TARGETplus siRNAs, but more selective inhibitors would strengthen the rationale behind considering SLC7A11 as a therapeutic target. Further studies are also needed to precisely elucidate how redox signaling controls cytoskeletal dynamics. Moreover, how other antioxidant systems/redox regulatory pathways support metastatic behavior remains to be investigated.

RESOURCE AVAILABILITY

Lead contact

Requests for further information and resources should be directed to and will be fulfilled by the lead contact, Victoria Sanz-Moreno (victoria.sanz-moreno@icr.ac.uk).

Materials availability

All unique/stable reagents generated in this study are available from the lead contact with a completed materials transfer agreement.

Data and code availability

- The MS-based metabolomics data presented in Figures 3E–3H have been deposited in the NIH Common Fund's National Metabolomics Data Repository (NMDR) via the Metabolomics Workbench (https://www.metabolomicsworkbench.org). The dataset is publicly available under the accession number NMDR: ST003925 and can be accessed directly through the project DOI upon publication: https://doi.org/10.21228/M8X84J. The accession number is also listed in the key resources table.
- This paper does not report original code.
- Any additional information required to reanalyze the data reported in this paper is available from the lead contact upon request.

ACKNOWLEDGMENTS

We thank Breast Cancer Now for funding this work as part of program funding to the Breast Cancer Now Toby Robins Research Center. The Cytoskeleton and Cancer Metastasis Team (V.S.-M., V.G., E.C.-M., J.B., D.D., J.A.J.M., O.M., M.L., A.V., and J.S.) was supported by ICR, Breast Cancer Now, UKRI, and Cancer Research UK (CRUK) C33043/A24478; the Barts Charity; Fundación Ramón Areces (ECM); World Wide Cancer Research 22-0329; and UKRI grant reference EP/X033392/. R.M.M. and X.M.-G. were supported by ISCIII/FEDER ''Una manera de hacer Europa'' FIS-PI1500711 and PI18/00573 (R.M.M.) and CIBERONC CB16/12/0023 (R.M.M. and X.M.-G.). A.T. and G.P. were supported by UKRI (MR/W012030/1 and MC_PC_MR/X013715/1). We thank Dr. Amaya Viros and Dr. Barrie Peck for helpful discussions.

AUTHOR CONTRIBUTIONS

Conceptualization, V.S.-M., V.G., and E.C.-M.; methodology, V.S.-M., E.C.-M., V.G., A.T., and G.P.; investigation, E.C.-M., V.G., J.B., D.D., J.A.J.M., A.V., M.L., and J.S.; validation, E.C.-M., O.M., and V.G.; writing – original draft, V.S.-M., V.G., and E.C.-M.; writing – review & editing, V.S.-M., V.G., and E.C.-M.; funding acquisition, V.S.-M., V.G., and E.C.-M.; resources, R.M.M. and X.M.-G.; supervision, V.S.-M.

DECLARATION OF INTERESTS

The authors declare no competing interests.

STAR★METHODS

Detailed methods are provided in the online version of this paper and include the following:

- KEY RESOURCES TABLE
- EXPERIMENTAL MODEL AND STUDY PARTICIPANT DETAILS
    - ○ Cell lines
    - ○ Intradermal tumors for generation of 4599 cell lines
    - ○ Animal-derived tissues
    - ○ Patient-derived tissues
- METHOD DETAILS
    - ○ Chemicals
    - ○ Antibodies
    - ○ Cell culture and treatments
    - ○ Cell morphology on collagen
    - ○ siRNA transfection
    - ○ Cell viability
    - ○ 3D invasion assay
    - ○ Invasive growth assay
    - ○ Western blotting

(E) Representative bright-field images of A375M2 cells seeded on a collagen I matrix and treated with GSH (10 mM), SLC7A11 inhibitor (erastin, 1 μM), or both for 24 h. Scale bar, 100 μm.
(F) Percentage of elongated cells for the indicated conditions in (E) ($n = 3$).
(G) Representative bright-field images of A375M2 cells seeded on a collagen I matrix and treated with GSH (10 mM), SLC7A11 inhibitor (sulfasalazine [SAS], 200 μM), or both for 24 h. Scale bar, 100 μm.
(H) Percentage of elongated cells for the conditions shown in (G) ($n = 3$).
For all graphs, statistical significance was determined using unpaired t test (A) and one-way ANOVA with Šídák's (B) or Tukey's correction (D, F, and H). Data are presented as mean ± SEM. For all graphs, $^{*}p < 0.05$, $^{**}p < 0.01$, $^{***}p < 0.001$, and $^{****}p < 0.0001$. See also Figure S4.

  - ○ Measurement of extracellular ROS
  - ○ Measurement of intracellular ROS
  - ○ Metabolite extraction and LC-MS analysis
  - ○ Analysis of gene expression from public databases
  - ○ Immunohistochemistry
- ● QUANTIFICATION AND STATISTICAL ANALYSIS

SUPPLEMENTAL INFORMATION

Supplemental information can be found online at https://doi.org/10.1016/j.celrep.2025.115939.

Received: September 12, 2024
Revised: April 12, 2025
Accepted: June 10, 2025
Published: July 11, 2025

REFERENCES

1. Sanderson, S.M., Gao, X., Dai, Z., and Locasale, J.W. (2019). Methionine metabolism in health and cancer: a nexus of diet and precision medicine. Nat. Rev. Cancer *19*, 625–637. https://doi.org/10.1038/s41568-019-0187-8.
2. Piskounova, E., Agathocleous, M., Murphy, M.M., Hu, Z., Huddlestun, S. E., Zhao, Z., Leitch, A.M., Johnson, T.M., DeBerardinis, R.J., and Morrison, S.J. (2015). Oxidative stress inhibits distant metastasis by human melanoma cells. Nature *527*, 186–191. https://doi.org/10.1038/nature15726.
3. Weems, A.D., Welf, E.S., Driscoll, M.K., Zhou, F.Y., Mazloom-Farsibaf, H., Chang, B.J., Murali, V.S., Gihana, G.M., Weiss, B.G., Chi, J., et al. (2023). Blebs promote cell survival by assembling oncogenic signalling hubs. Nature *615*, 517–525. https://doi.org/10.1038/s41586-023-05758-6.
4. Maiques, O., and Sanz-Moreno, V. (2022). Location, location, location: Melanoma cells "living at the edge. Exp. Dermatol. *31*, 82–88. https://doi.org/10.1111/exd.14423.
5. Lammermann, T., and Sixt, M. (2009). Mechanical modes of 'amoeboid' cell migration. Curr. Opin. Cell Biol. *21*, 636–644. https://doi.org/10.1016/j.ceb.2009.05.003.
6. Graziani, V., Rodriguez-Hernandez, I., Maiques, O., and Sanz-Moreno, V. (2022). The amoeboid state as part of the epithelial-to-mesenchymal transition programme. Trends Cell Biol. *32*, 228–242. https://doi.org/10.1016/j.tcb.2021.10.004.
7. Sanz-Moreno, V., Gaggioli, C., Yeo, M., Albrengues, J., Wallberg, F., Viros, A., Hooper, S., Mitter, R., Féral, C.C., Cook, M., et al. (2011). ROCK and JAK1 signaling cooperate to control actomyosin contractility in tumor cells and stroma. Cancer Cell *20*, 229–245. https://doi.org/10.1016/j.ccr.2011.06.018.
8. Georgouli, M., Herraiz, C., Crosas-Molist, E., Fanshawe, B., Maiques, O., Perdrix, A., Pandya, P., Rodriguez-Hernandez, I., Ilieva, K.M., Cantelli, G., et al. (2019). Regional Activation of Myosin II in Cancer Cells Drives Tumor Progression via a Secretory Cross-Talk with the Immune Microenvironment. Cell *176*, 757–774.e23. https://doi.org/10.1016/j.cell.2018.12.038.
9. Orgaz, J.L., Crosas-Molist, E., Sadok, A., Perdrix-Rosell, A., Maiques, O., Rodriguez-Hernandez, I., Monger, J., Mele, S., Georgouli, M., Bridgeman, V., et al. (2020). Myosin II Reactivation and Cytoskeletal Remodeling as a Hallmark and a Vulnerability in Melanoma Therapy Resistance. Cancer Cell *37*, 85–103.e9. https://doi.org/10.1016/j.ccell.2019.12.003.
10. Sanz-Moreno, V., Gadea, G., Ahn, J., Paterson, H., Marra, P., Pinner, S., Sahai, E., and Marshall, C.J. (2008). Rac activation and inactivation control plasticity of tumor cell movement. Cell *135*, 510–523. https://doi.org/10.1016/j.cell.2008.09.043.
11. Gadea, G., Sanz-Moreno, V., Self, A., Godi, A., and Marshall, C.J. (2008). DOCK10-mediated Cdc42 activation is necessary for amoeboid invasion of melanoma cells. Curr. Biol. *18*, 1456–1465. https://doi.org/10.1016/j.cub.2008.08.053.
12. Rodriguez-Hernandez, I., Maiques, O., Kohlhammer, L., Cantelli, G., Perdrix-Rosell, A., Monger, J., Fanshawe, B., Bridgeman, V.L., Karagiannis, S.N., Penin, R.M., et al. (2020). WNT11-FZD7-DAAM1 signalling supports tumour initiating abilities and melanoma amoeboid invasion. Nat. Commun. *11*, 5315. https://doi.org/10.1038/s41467-020-18951-2.
13. Gao, Y., Wang, Z., Hao, Q., Li, W., Xu, Y., Zhang, J., Zhang, W., Wang, S., Liu, S., Li, M., et al. (2017). Loss of ERalpha induces amoeboid-like migration of breast cancer cells by downregulating vinculin. Nat. Commun. *8*, 14483. https://doi.org/10.1038/ncomms14483.
14. Crosas-Molist, E., Bertran, E., Rodriguez-Hernandez, I., Herraiz, C., Cantelli, G., Fabra, À., Sanz-Moreno, V., and Fabregat, I. (2017). The NADPH oxidase NOX4 represses epithelial to amoeboid transition and efficient tumour dissemination. Oncogene *36*, 3002–3014. https://doi.org/10.1038/onc.2016.454.
15. Lopez-Luque, J., Bertran, E., Crosas-Molist, E., Maiques, O., Malfettone, A., Caja, L., Serrano, T., Ramos, E., Sanz-Moreno, V., and Fabregat, I. (2019). Downregulation of Epidermal Growth Factor Receptor in hepatocellular carcinoma facilitates Transforming Growth Factor-beta-induced epithelial to amoeboid transition. Cancer Lett. *464*, 15–24. https://doi.org/10.1016/j.canlet.2019.08.011.
16. Samain, R., Maiques, O., Monger, J., Lam, H., Candido, J., George, S., Ferrari, N., Kohlhammer, L., Lunetto, S., Varela, A., et al. (2023). CD73 controls Myosin II-driven invasion, metastasis, and immunosuppression in amoeboid pancreatic cancer cells. Sci. Adv. *9*, eadi0244. https://doi.org/10.1126/sciadv.adi0244.
17. Valcarcel-Jimenez, L., Macchia, A., Crosas-Molist, E., Schaub-Clerigué, A., Camacho, L., Martín-Martín, N., Cicogna, P., Viera-Bardón, C., Fernández-Ruiz, S., Rodriguez-Hernandez, I., et al. (2019). PGC1alpha Suppresses Prostate Cancer Cell Invasion through ERRalpha Transcriptional Control. Cancer Res. *79*, 6153–6165. https://doi.org/10.1158/0008-5472.CAN-19-1231.
18. Lehmann, S., Te Boekhorst, V., Odenthal, J., Bianchi, R., van Helvert, S., Ikenberg, K., Ilina, O., Stoma, S., Xandry, J., Jiang, L., et al. (2017). Hypoxia Induces a HIF-1-Dependent Transition from Collective-to-Amoeboid Dissemination in Epithelial Cancer Cells. Curr. Biol. *27*, 392–400. https://doi.org/10.1016/j.cub.2016.11.057.
19. Barcelo, J., Samain, R., and Sanz-Moreno, V. (2023). Preclinical to clinical utility of ROCK inhibitors in cancer. Trends Cancer *9*, 250–263. https://doi.org/10.1016/j.trecan.2022.12.001.
20. Maiques, O., Fanshawe, B., Crosas-Molist, E., Rodriguez-Hernandez, I., Volpe, A., Cantelli, G., Boehme, L., Orgaz, J.L., Mardakheh, F.K., Sanz-Moreno, V., and Fruhwirth, G.O. (2021). A preclinical pipeline to evaluate migrastatics as therapeutic agents in metastatic melanoma. Br. J. Cancer *125*, 699–713. https://doi.org/10.1038/s41416-021-01442-6.
21. Drapela, S., and Gomes, A.P. (2021). Metabolic requirements of the metastatic cascade. Curr. Opin. Syst. Biol. *28*, 100381. https://doi.org/10.1016/j.coisb.2021.100381.
22. Crosas-Molist, E., Samain, R., Kohlhammer, L., Orgaz, J.L., George, S.L., Maiques, O., Barcelo, J., and Sanz-Moreno, V. (2022). Rho GTPase signaling in cancer progression and dissemination. Physiol. Rev. *102*, 455–510. https://doi.org/10.1152/physrev.00045.2020.
23. Herraiz, C., Calvo, F., Pandya, P., Cantelli, G., Rodriguez-Hernandez, I., Orgaz, J.L., Kang, N., Chu, T., Sahai, E., and Sanz-Moreno, V. (2016). Reactivation of p53 by a Cytoskeletal Sensor to Control the Balance Between DNA Damage and Tumor Dissemination. J. Natl. Cancer Inst. *108*, djv289. https://doi.org/10.1093/jnci/djv289.
24. Crosas-Molist, E., Graziani, V., Maiques, O., Pandya, P., Monger, J., Samain, R., George, S.L., Malik, S., Salise, J., Morales, V., et al. (2023). AMPK is a mechano-metabolic sensor linking cell adhesion and mitochondrial dynamics to Myosin-dependent cell migration. Nat. Commun. *14*, 2740. https://doi.org/10.1038/s41467-023-38292-0.

25. Jyotsana, N., Ta, K.T., and DelGiorno, K.E. (2022). The Role of Cystine/Glutamate Antiporter SLC7A11/xCT in the Pathophysiology of Cancer. Front. Oncol. *12*, 858462. https://doi.org/10.3389/fonc.2022.858462.

26. Parker, J.L., Deme, J.C., Kolokouris, D., Kuteyi, G., Biggin, P.C., Lea, S.M., and Newstead, S. (2021). Molecular basis for redox control by the human cystine/glutamate antiporter system xc. Nat. Commun. *12*, 7147. https://doi.org/10.1038/s41467-021-27414-1.

27. Seibt, T.M., Proneth, B., and Conrad, M. (2019). Role of GPX4 in ferroptosis and its pharmacological implication. Free Radic. Biol. Med. *133*, 144–152. https://doi.org/10.1016/j.freeradbiomed.2018.09.014.

28. Te Boekhorst, V., Jiang, L., Mahlen, M., Meerlo, M., Dunkel, G., Durst, F. C., Yang, Y., Levine, H., Burgering, B.M.T., and Friedl, P. (2022). Calpain-2 regulates hypoxia/HIF-induced plasticity toward amoeboid cancer cell migration and metastasis. Curr. Biol. *32*, 412–427.e418. https://doi.org/10.1016/j.cub.2021.11.040.

29. Lu, S.C. (2013). Glutathione synthesis. Biochim. Biophys. Acta *1830*, 3143–3153. https://doi.org/10.1016/j.bbagen.2012.09.008.

30. Ishimoto, T., Nagano, O., Yae, T., Tamada, M., Motohara, T., Oshima, H., Oshima, M., Ikeda, T., Asaba, R., Yagi, H., et al. (2011). CD44 variant regulates redox status in cancer cells by stabilizing the xCT subunit of system xc(-) and thereby promotes tumor growth. Cancer Cell *19*, 387–400. https://doi.org/10.1016/j.ccr.2011.01.038.

31. Lin, W., Wang, C., Liu, G., Bi, C., Wang, X., Zhou, Q., and Jin, H. (2020). SLC7A11/xCT in cancer: biological functions and therapeutic implications. Am. J. Cancer Res. *10*, 3106–3126.

32. Shin, S.S., Jeong, B.S., Wall, B.A., Li, J., Shan, N.L., Wen, Y., Goydos, J. S., and Chen, S. (2018). Participation of xCT in melanoma cell proliferation in vitro and tumorigenesis in vivo. Oncogenesis *7*, 86. https://doi.org/10.1038/s41389-018-0098-7.

33. Weiss, F., Atlasy, N., van Reijmersdal, V., Stunnenberg, H., Hulsbergen-Veelken, C., and Friedl, P. (2022). 3D spheroid culture to examine adaptive therapy response in invading tumor cells. In Vitro Model *1*, 463–471. https://doi.org/10.1007/s44164-022-00040-x.

34. Clark, E.A., Golub, T.R., Lander, E.S., and Hynes, R.O. (2000). Genomic analysis of metastasis reveals an essential role for RhoC. Nature *406*, 532–535. https://doi.org/10.1038/35020106.

35. Orgaz, J.L., Pandya, P., Dalmeida, R., Karagiannis, P., Sanchez-Laorden, B., Viros, A., Albrengues, J., Nestle, F.O., Ridley, A.J., Gaggioli, C., et al. (2014). Diverse matrix metalloproteinase functions regulate cancer amoeboid migration. Nat. Commun. *5*, 4255. https://doi.org/10.1038/ncomms5255.

36. Fotiadis, D., Kanai, Y., and Palacín, M. (2013). The SLC3 and SLC7 families of amino acid transporters. Mol. Aspects Med. *34*, 139–158. https://doi.org/10.1016/j.mam.2012.10.007.

37. Sadok, A., McCarthy, A., Caldwell, J., Collins, I., Garrett, M.D., Yeo, M., Hooper, S., Sahai, E., Kuemper, S., Mardakheh, F.K., and Marshall, C.J. (2015). Rho kinase inhibitors block melanoma cell migration and inhibit metastasis. Cancer Res. *75*, 2272–2284. https://doi.org/10.1158/0008-5472.CAN-14-2156.

38. Meeth, K., Wang, J.X., Micevic, G., Damsky, W., and Bosenberg, M.W. (2016). The YUMM lines: a series of congenic mouse melanoma cell lines with defined genetic alterations. Pigment Cell Melanoma Res. *29*, 590–597. https://doi.org/10.1111/pcmr.12498.

39. Kashif, M., Yao, H., Schmidt, S., Chen, X., Truong, M., Tüksammel, E., Liu, Y., and Bergo, M.O. (2023). ROS-lowering doses of vitamins C and A accelerate malignant melanoma metastasis. Redox Biol. *60*, 102619. https://doi.org/10.1016/j.redox.2023.102619.

40. Cui, T., Li, X., Shu, Y., Huang, X., Wang, Y., and Zhang, W. (2018). Utilizing glutathione-triggered nanoparticles to enhance chemotherapy of lung cancer by reprograming the tumor microenvironment. Int. J. Pharm. *552*, 16–26. https://doi.org/10.1016/j.ijpharm.2018.09.050.

41. Zhao, M., Liu, Q., Gong, Y., Xu, X., Zhang, C., Liu, X., Zhang, C., Guo, H., Zhang, X., Gong, Y., and Shao, C. (2016). GSH-dependent antioxidant defense contributes to the acclimation of colon cancer cells to acidic microenvironment. Cell Cycle *15*, 1125–1133. https://doi.org/10.1080/15384101.2016.1158374.

42. Koppula, P., Zhuang, L., and Gan, B. (2021). Cystine transporter SLC7A11/xCT in cancer: ferroptosis, nutrient dependency, and cancer therapy. Protein Cell *12*, 599–620. https://doi.org/10.1007/s13238-020-00789-5.

43. Rossi, R., Dalle-Donne, I., Milzani, A., and Giustarini, D. (2006). Oxidized forms of glutathione in peripheral blood as biomarkers of oxidative stress. Clin. Chem. *52*, 1406–1414. https://doi.org/10.1373/clinchem.2006.067793.

44. Bakalova, R., Aoki, I., Zhelev, Z., and Higashi, T. (2022). Cellular redox imbalance on the crossroad between mitochondrial dysfunction, senescence, and proliferation. Redox Biol. *53*, 102337. https://doi.org/10.1016/j.redox.2022.102337.

45. Mitric, A., and Castellano, I. (2023). Targeting gamma-glutamyl transpeptidase: A pleiotropic enzyme involved in glutathione metabolism and in the control of redox homeostasis. Free Radic. Biol. Med. *208*, 672–683. https://doi.org/10.1016/j.freeradbiomed.2023.09.020.

46. Du, Y., and Guo, Z. (2022). Recent progress in ferroptosis: inducers and inhibitors. Cell Death Discov. *8*, 501. https://doi.org/10.1038/s41420-022-01297-7.

47. Yang, Y., Luo, M., Zhang, K., Zhang, J., Gao, T., Connell, D.O., Yao, F., Mu, C., Cai, B., Shang, Y., and Chen, W. (2020). Nedd4 ubiquitylates VDAC2/3 to suppress erastin-induced ferroptosis in melanoma. Nat. Commun. *11*, 433. https://doi.org/10.1038/s41467-020-14324-x.

48. Linares, V., Alonso, V., and Domingo, J.L. (2011). Oxidative stress as a mechanism underlying sulfasalazine-induced toxicity. Expert Opin. Drug Saf. *10*, 253–263. https://doi.org/10.1517/14740338.2011.529898.

49. Lee, J., and Roh, J.L. (2023). Targeting GPX4 in human cancer: Implications of ferroptosis induction for tackling cancer resilience. Cancer Lett. *559*, 216119. https://doi.org/10.1016/j.canlet.2023.216119.

50. Jiang, X., Yu, M., Wang, W.K., Zhu, L.Y., Wang, X., Jin, H.C., and Feng, L. F. (2024). The regulation and function of Nrf2 signaling in ferroptosis-activated cancer therapy. Acta Pharmacol. Sin. *45*, 2229–2240. https://doi.org/10.1038/s41401-024-01336-2.

51. Zheng, J., and Conrad, M. (2025). Ferroptosis: when metabolism meets cell death. Physiol. Rev. *105*, 651–706. https://doi.org/10.1152/physrev.00031.2024.

52. Burbelo, P.D., Miyamoto, S., Utani, A., Brill, S., Yamada, K.M., Hall, A., and Yamada, Y. (1995). p190-B, a new member of the Rho GAP family, and Rho are induced to cluster after integrin cross-linking. J. Biol. Chem. *270*, 30919–30926. https://doi.org/10.1074/jbc.270.52.30919.

53. Zhang, J., Ye, Z.W., Singh, S., Townsend, D.M., and Tew, K.D. (2018). An evolving understanding of the S-glutathionylation cycle in pathways of redox regulation. Free Radic. Biol. Med. *120*, 204–216. https://doi.org/10.1016/j.freeradbiomed.2018.03.038.

54. Dalle-Donne, I., Giustarini, D., Rossi, R., Colombo, R., and Milzani, A. (2003). Reversible S-glutathionylation of Cys 374 regulates actin filament formation by inducing structural changes in the actin molecule. Free Radic. Biol. Med. *34*, 23–32. https://doi.org/10.1016/s0891-5849(02)01182-6.

55. Sakai, J., Li, J., Subramanian, K.K., Mondal, S., Bajrami, B., Hattori, H., Jia, Y., Dickinson, B.C., Zhong, J., Ye, K., et al. (2012). Reactive oxygen species-induced actin glutathionylation controls actin dynamics in neutrophils. Immunity *37*, 1037–1049. https://doi.org/10.1016/j.immuni.2012.08.017.

56. Uemura, T., Tsaprailis, G., and Gerner, E.W. (2019). GSTPi stimulates caveolin-1-regulated polyamine uptake via actin remodeling. Oncotarget *10*, 5713–5723. https://doi.org/10.18632/oncotarget.27192.

57. Li, X., Wu, J., Zhang, X., and Chen, W. (2018). Glutathione reductase-mediated thiol oxidative stress suppresses metastasis of murine

melanoma cells. Free Radic. Biol. Med. *129*, 256–267. https://doi.org/10.1016/j.freeradbiomed.2018.07.025.

58. Shin, C.S., Mishra, P., Watrous, J.D., Carelli, V., D'Aurelio, M., Jain, M., and Chan, D.C. (2017). The glutamate/cystine xCT antiporter antagonizes glutamine metabolism and reduces nutrient flexibility. Nat. Commun. *8*, 15074. https://doi.org/10.1038/ncomms15074.
59. Dhomen, N., Reis-Filho, J.S., da Rocha Dias, S., Hayward, R., Savage, K., Delmas, V., Larue, L., Pritchard, C., and Marais, R. (2009). Oncogenic Braf induces melanocyte senescence and melanoma in mice. Cancer Cell *15*, 294–303. https://doi.org/10.1016/j.ccr.2009.02.022.
60. Day, C.P., Carter, J., Bonomi, C., Esposito, D., Crise, B., Ortiz-Conde, B., Hollingshead, M., and Merlino, G. (2009). Lentivirus-mediated bifunctional cell labeling for in vivo melanoma study. Pigment Cell Melanoma Res. *22*, 283–295. https://doi.org/10.1111/j.1755-148X.2009.00545.x.
61. Maiques, O., Sallan, M.C., Laddach, R., Pandya, P., Varela, A., Crosas-Molist, E., Barcelo, J., Courbot, O., Liu, Y., Graziani, V., et al. (2025). Matrix mechano-sensing at the invasive front induces a cytoskeletal and transcriptional memory supporting metastasis. Nat. Commun. *16*, 1394. https://doi.org/10.1038/s41467-025-56299-7.
62. Jung-Garcia, Y., Maiques, O., Monger, J., Rodriguez-Hernandez, I., Fanshawe, B., Domart, M.C., Renshaw, M.J., Marti, R.M., Matias-Guiu, X., Collinson, L.M., et al. (2023). LAP1 supports nuclear adaptability during constrained melanoma cell migration and invasion. Nat. Cell Biol. *25*, 108–119. https://doi.org/10.1038/s41556-022-01042-3.
63. Del Duca, D., Werbowetski, T., and Del Maestro, R.F. (2004). Spheroid preparation from hanging drops: characterization of a model of brain tumor invasion. J. Neuro Oncol. *67*, 295–303. https://doi.org/10.1023/b:neon.0000024220.07063.70.
64. Hoek, K., Rimm, D.L., Williams, K.R., Zhao, H., Ariyan, S., Lin, A., Kluger, H.M., Berger, A.J., Cheng, E., Trombetta, E.S., et al. (2004). Expression profiling reveals novel pathways in the transformation of melanocytes to melanomas. Cancer Res. *64*, 5270–5282. https://doi.org/10.1158/0008-5472.CAN-04-0731.
65. Hoek, K.S., Schlegel, N.C., Brafford, P., Sucker, A., Ugurel, S., Kumar, R., Weber, B.L., Nathanson, K.L., Phillips, D.J., Herlyn, M., et al. (2006). Metastatic potential of melanomas defined by specific gene expression profiles with no BRAF signature. Pigment Cell Res. *19*, 290–302. https://doi.org/10.1111/j.1600-0749.2006.00322.x.
66. Kabbarah, O., Nogueira, C., Feng, B., Nazarian, R.M., Bosenberg, M., Wu, M., Scott, K.L., Kwong, L.N., Xiao, Y., Cordon-Cardo, C., et al. (2010). Integrative genome comparison of primary and metastatic melanomas. PLoS One *5*, e10770. https://doi.org/10.1371/journal.pone.0010770.
67. Talantov, D., Mazumder, A., Yu, J.X., Briggs, T., Jiang, Y., Backus, J., Atkins, D., and Wang, Y. (2005). Novel genes associated with malignant melanoma but not benign melanocytic lesions. Clin. Cancer Res. *11*, 7234–7242. https://doi.org/10.1158/1078-0432.CCR-05-0683.
68. Riker, A.I., Enkemann, S.A., Fodstad, O., Liu, S., Ren, S., Morris, C., Xi, Y., Howell, P., Metge, B., Samant, R.S., et al. (2008). The gene expression profiles of primary and metastatic melanoma yields a transition point of tumor progression and metastasis. BMC Med. Genomics *1*, 13. https://doi.org/10.1186/1755-8794-1-13.
69. Bankhead, P., Loughrey, M.B., Fernández, J.A., Dombrowski, Y., McArt, D.G., Dunne, P.D., McQuaid, S., Gray, R.T., Murray, L.J., Coleman, H. G., et al. (2017). QuPath: Open source software for digital pathology image analysis. Sci. Rep. *7*, 16878. https://doi.org/10.1038/s41598-017-17204-5.

STAR★METHODS

KEY RESOURCES TABLE

REAGENT or RESOURCE	SOURCE	IDENTIFIER
Antibodies		
Rabbit Ab anti-pThr18/Ser19-MLC2	Cell Signaling Technology	Cat# 3674; RRID: AB_2147464
Rabbit Ab anti-MLC2	Cell Signaling Technology	Cat# 3672; RRID: AB_10692513
Mouse mAb anti-GAPDH (6C5)	Millipore	Cat# MAB374; RRID: AB_2107445
Rabbit mAb anti-xCT/SLC7A11 (D2M7A)	Cell Signaling Technology	Cat# 12691; RRID: AB_2687474
Rabbit Ab anti-xCT/SLC7A11	Cell Signaling Technology	Cat# 98051; RRID: AB_2800296
Rabbit Ab anti-Glutathione Peroxidase 4	Abcam	Cat# ab125066; RRID: AB_10973849
Biological samples		
Human melanoma tissue microarrays	Hospital Universitari Arnau de Vilanova in Lleida, Spain	N/A
Chemicals, peptides, and recombinant proteins		
(±)-Blebbistatin	Calbiochem	203390; CAS: 674289-55-5
H1152	Calbiochem	555550; CAS: 871543-07-6
GSK269962A	Axon MedChem	1167; CAS: 850664-21-0
Menadione	Sigma	M5625; CAS: 58-27-5
L-Glutathione reduced	Sigma	G6013; CAS: 70-18-8
Erastin	Sigma	E7781; CAS: 571203-78-6
SAS	Sigma	S0883; CAS: 599-79-1
L-BSO	Sigma	B2515; CAS: 83730-53-4
PureCol type I bovine collagen	Advanced BioMatrix	5005
FibriCol type I bovine collagen	Advanced BioMatrix	5133
MitoSOX	ThermoFisher	M36008
Amplex^{TM} Red Hydrogen Peroxide/Peroxidase	ThermoFisher	A22188
Labeled Glutathione (GSH)	CK Isotopes Limited	CNLM-6245-50; CAS Number Labeled: 815610-65-2
Deposited data		
Mass spectrometry for metabolomics data	This paper	https://doi.org/10.21228/M8X84J; NMDR: ST003925
Experimental models: Cell lines		
Human: A375P	Richard Hynes (HHMI, MIT, USA)	N/A
Human: A375M2	Richard Hynes (HHMI, MIT, USA)	N/A
Mouse: 4599	Amine Sadok (ICR, UK) and Richard Marais (CRUK Manchester Institute, UK)	N/A
Mouse: 4599-TB	Oscar Maiques (BCI, UK)	https://doi.org/10.1038/s41467-025-56299-7
Mouse: 4599-IF	Oscar Maiques (BCI, UK)	https://doi.org/10.1038/s41467-025-56299-7
Mouse: YUMM1.1 eGFP-Luc	Hector Peinado (CNIO, Spain)	N/A
Mouse: YUMM1.7	ATCC	ATCC: CRL-3362
Mouse: YUMM1.7 eGFP-Luc	This study	N/A
Oligonucleotides		
siGENOME Human SLC7A11 siRNA SMARTPool: (D-007612-01) 5′-GGAAGUCUUUGGUCCAUUA-3’; (D-007612-02) 5′-GGAGUUAUGCA GCUAAUUA-3’; (D-007612-03) 5′-GGGAACA ACUAUAAAGAAA-3’; (D-007612-04) 5′-UGACAA AUGUGGCCUACUU-3′	Horizon Discovery	M-007612-01-0005

(*Continued on next page*)

Continued

REAGENT or RESOURCE	SOURCE	IDENTIFIER
siGENOME non-targeting Control (Scramble): 5′-UGGUUUACAUGUCGACUAA-3′	Horizon Discovery	D-001210-05-05
ON-TARGET plus Human SLC7A11 siRNA: (J-007612-09, OT-9) 5′-UUGUAGAGCUUG CGUAGAA-3’; (J-007612-10, OT-10) 5′-CGGCAAACUUAUUGGGUCU-3′	Horizon Discovery	LQ-007612-01-0002
ON-TARGET (OT) non-targeting Control (Scramble): 5′-UGGUUUACAUGUCGACUAA-3′	Horizon Discovery	D-001810-01-05
Recombinant DNA		
pFUGW-FerH-ffLuc2-eGFP	Addgene	Addgene plasmid #71393
Software and algorithms		
Fiji	http://fiji.sc	RRID: SCR_002285
GraphPad Prism 8	http://www.graphpad.com/	RRID:SCR_002798
FlowJo	https://www.flowjo.com/solutions/flowjo	RRID:SCR_008520
QuPath	https://qupath.github.io/	RRID:SCR_018257
Morpheus	https://software.broadinstitute.org/morpheus/	RRID: SCR_017386
Agilent Masshunter Workstation Data Acquisition software	https://www.agilent.com/en/product/software-informatics/mass-spectrometry-software/data-acquisition	RRID:SCR_016657
ZEISS ZEN Black	https://www.zeiss.com/microscopy/us/products/software/zeiss-zen.html	RRID:SCR_018163
Gene Pattern	http://www.broadinstitute.org/cancer/software/genepattern/	RRID:SCR_003201

EXPERIMENTAL MODEL AND STUDY PARTICIPANT DETAILS

Cell lines

A375P and A375M2 human melanoma cell lines were obtained from Prof. Richard Hynes (HHMI, MIT, USA). The 4599 murine melanoma cell line, harboring the *Braf∧LSL-V600E/+; Tyr::CreERT2∧+/o* genotype, was a gift from Prof. Richard Marais (formerly Cancer Research UK Manchester Institute) and was derived from a C57BL/6 mouse.[59] YUMM1.1 eGFP-LUC cells were kindly provided by Dr. Hector Peinado (CNIO, Spain). YUMM1.7 parental cells were obtained from ATCC (CRL-3362).

For the generation of YUMM1.7 eGFP-LUC cells, YUMM1.7 cells were transduced with a lentiviral vector encoding enhanced green fluorescent protein (eGFP) and firefly luciferase 2 (ffLuc2), both driven by the human ferritin heavy chain (FerH) promoter. The plasmid pFUGW-FerH-ffLuc2-eGFP was deposited by Dr. Glenn Merlino laboratory[60] (Addgene plasmid #71393; http://n2t.net/addgene:71393). Lentiviral particles were produced by transfecting HEK293 cells in T75 flasks with 6.25 μg of pFUGW-FerH-ffLuc2-eGFP, 6.25 μg of packaging plasmid psPAX2, and 2.5 μg of envelope plasmid pMD2.G (Addgene) using Opti-MEM (GIBCO) and Lipofectamine 2000 (Invitrogen), following the manufacturer’s instructions. Seventy-two hours post-transfection, viral supernatant was harvested, filtered through a 0.45 μm PES filter to remove cell debris, and stored at −80°C in single-use aliquots to avoid repeated freeze–thaw cycles. Parental YUMM1.7 cells were seeded at 50–70% confluency and incubated with the lentiviral supernatant. Transduction efficiency was evaluated by assessing eGFP expression via flow cytometry and luciferase activity using a luciferase reporter assay (Promega). Successfully transduced cells were expanded and used for downstream *in vitro* and *in vivo* experiments.

All cell lines were grown at 37°C and 10% CO_2 in DMEM supplemented with 10% FBS and 1% penicillin/streptomycin (all from GIBCO), except YUMM1.1 and YUMM1.7 cells, which were also supplemented with 1x NEAA. All cell lines were kept in culture for a maximum of three to four passages and cell phenotypes were verified routinely. All cell lines were authenticated using short tandem repeat DNA profiling and tested negative for mycoplasma contamination prior to use.

Intradermal tumors for generation of 4599 cell lines

These cell lines were generated in a previous study.[61] All animals were maintained under specific pathogen-free conditions and handled in accordance with the Institutional Committees on Animal Welfare of the UK Home Office (The Home Office Animals

Scientific Procedures Act, 1986). All animal experiments were approved by the Ethical Review Process Committees at Barts Cancer Institute and carried out under licences from the Home Office, UK. Animals were housed in groups of 4–5 mice per cage with access to food and water *ad libitum*. Mice were maintained on an alternating 12 h light-dark cycle, with controlled room temperature (21 ± 1°C) and relative humidity (40–60%). 200,000 mouse melanoma 4599 cells in 30 μL PBS were injected intradermally orthotopically into the skin of 6–8 weeks old NXG (NOD-Prkdcscid-Il2rgtm1/Rj) female mice (Janvier-Labs). At the endpoint (28 days), 4599 TB and IF derived cells were isolated from the intradermal tumors.

Animal-derived tissues

A375P tumors were generated in a previous study.[62] Briefly, 2×10^5 A375P cells suspended in 50 μL of $PBS^{-/-}$ were injected intradermally into the skin of 6–8-week-old female NXG (NOD-Prkdc∧scid∧ Il2rg∧tm1∧/Rj) mice. Each mouse received two injections, one per flank, yielding two tumors per animal. A total of eight mice were used (n = 8), resulting in 16 tumors. These tumors were collected and used in this study for immunohistological analysis. All mice were maintained under the same housing and welfare conditions, in accordance with UK Home Office guidelines as described above.

Patient-derived tissues

Tumors were classified following the most recent World Health Organization criteria. Tumor samples were processed by IRB Lleida (PT17/0015/0027) and HUB-ICO-IDIBELL (PT17/0015/0024) Biobanks integrated in the Spanish National Biobank Network and Xarxa de Bancs de Tumors de Catalunya following standard operating procedures with the appropriate approval of the Ethics and Scientific Committee. Samples were collected with specific informed consent, in accordance with the Helsinki Declaration.

Two cohorts were evaluated for tissue microarrays including FFPE biopsies of human primary melanomas and metastases were included in the case series. Cohort A originally included 40 patients. Of these, 20 were retained for analysis: 12 with primary tumors and 8 with metastatic tumors. The age of patients in the unmatched Cohort A ranged from 32 to ≥89 years, with a male-to-female ratio of 1:1 (see Table S1 in the supplementary information file). These patients were not matched based on any specific criteria. Cohort B originally consisted of 29 patients. After exclusions, 20 patients remained, each with a primary tumor and corresponding metastasis. The age of patients in the matched Cohort B ranged from ≤24 to 87 years, with a male-to-female ratio of 1:1. (see Table S2 in the supplementary information file) in the supplementary information file). Patients were excluded from both cohorts due to tissue exhaustion or the absence of tissue microarray (TMA) data. Each biopsy was represented by two cores (1 mm diameter) from the tumor body (TB) and two cores from the invasive front (IF) areas.[24]

METHOD DETAILS

Chemicals

Compounds/inhibitors: H1152 (5μM, Calbiochem #555550), GSK269962A (1μM, Axon MedChem 1167), Blebbistatin (25μM, Calbiochem 203390), Menadione (10μM, Sigma M5625), L-Glutathione reduced (10mM, Sigma G6013), erastin (1μM unless otherwise stated, Sigma E7781), SAS (200μM, Sigma S0883) and L-BSO (250μM, Sigma B2515).

Reagents: PureCol type I bovine collagen (Advanced BioMatrix, #5005), FibriCol type I bovine collagen (Advanced BioMatrix, #5133), MitoSOX (5μM), Alexa Fluor 546-phalloidin (Thermo Fisher A22283).

Antibodies

SLC7A11 (Cell Signaling Technology #12691 for human samples, #98051 for mouse samples), pThr18/Ser19-MLC2 (Cell Signaling Technology #3674), MLC2 (Cell Signaling Technology #3672), GAPDH (Millipore MAB374), GPX4 (Abcam, ab125066).

Cell culture and treatments

For cell culture on thick layers of collagen I, fibrillar bovine dermal collagen (PureCol, Advanced BioMatrix) was prepared at 1.7 mg/mL in DMEM (300μL/T24 well; 100μL/T96 well). Cells were seeded on top of collagen in medium containing 10% FBS, allowed to adhere for 24 h and medium changed to 1% serum with the corresponding treatment for 24 h (unless otherwise stated).

Cell morphology on collagen

Cell morphology of cells seeded on collagen matrices was quantified on still phase-contrast images using ImageJ. Cell morphology was assessed using the morphology descriptor tool "roundness" after manually drawing around the cell. Values closer to 1 represent rounded morphology; values closer to 0 represent more spindle-shaped cells. Cells with a roundness index below 0.6 were considered elongated to calculate the percentage of elongated cells.

siRNA transfection

Reverse transfection was used to transiently silence SLC7A11. 2.5×10^5 cells/well were seeded in complete media (DMEM 10%FBS) in 6-well plates with a mix containing 20nM siGenome SmartPool or individual OTs (On Target) siRNA oligonucleotides (Dharmacon), OptiMEM (GIBCO) and Lipofectamine 2000 (Invitrogen). Non-targeting siRNA was used as control. Forty-eight hours after transfection cells were split and seeded for the downstream experiments (on collagen gels from 24-well plates for cell morphology and from 12-well plates for western blotting).

Cell viability

Cell viability was analyzed through crystal violet staining. Cells were seeded in 24-well plates. After the treatment and time indicated, media was removed, cells were washed with PBS and the remaining viable adherent cells were fixed with formaldehyde 1% for 15 min, washed again twice with PBS and stained with crystal violet solution (0.25%) for 15 min. Following this, the staining solution was removed, and cells were washed several times with distilled water until the excess staining was eliminated. Plates were air-dried, and the stained cells were resuspended in 10% acetic acid for quantification. Absorbance was measured at 595nm.

3D invasion assay

For 3D invasion assays, cells were resuspended in serum-free bovine collagen I solution at 1.7 mg/mL to a final concentration of 25,000 cells per 100 μL of matrix and spun down, in a 96-well plate. After the matrix was polymerized, 1% FBS-containing media was added on top of the matrix. After 24 h cells were fixed, stained with Hoechst and imaged using a Super Resolution Spinning Disk (TIRF/STORM/SoRa) microscope. Invasion was calculated as number of invading cells at 60 μm divided by the number of cells at the bottom.

Invasive growth assay

A375M2 spheroids assay: A375M2 cells grown in DMEM media supplemented with 10% FBS were pelleted 24 h after transfection with siScramble or siSLC7A11. Media was then changed to DMEM/F12 supplemented with 1X B27 supplement, 20 ng/mL EGF, 20 ng/mL FGF and 4 μg/mL of Heparin and spheroids were incubated at 37°C, 10% CO_2 for 72 h in 1.5 mL Eppendorf. 96 h post-transfection, spheroids were transferred to ultra-low attachment 96-well plates containing 100 μL of a collagen I matrix (Fibricol, 2.3 mg/mL) and left to polymerise for four hours, when supplemented DMEM media was added. After this time, images were taken of spheroids for day 0 (day 4 post-transfection) and left in the incubator at 37°C, 10% CO_2 for 72 h, where spheroids were fixed in 12% PFA for two hours and washed three times in PBS. Pictures were taken again for day 3 (day 7 post-transfection) using EVOS M7000 in brightfield. Spheroid growth was calculated in FIJI (ImageJ) by dividing the area of the spheroids at day 3 vs. day 0 and calculated as a fold change.

YUMM 1.7 spheroid assay: Spheroid cell culture was performed using the hanging drop method, as described previously by Del Duca et al..[63] Briefly, 1 000 cells/drop were seeded in hanging drops for 72h. Once formed, spheroids were collected and seeded in 100μL collagen I solution (3.5mg/ml high concentration FibriCol type I bovine collagen (Advanced BioMatrix, #5133)) in ultra-low attachment 96-well plates. After allowing the gels to polymerise for 2h at 37°C, 10% CO_2, day 0 brightfield images were taken using a ZEISS Axio Observer microscope. Then, indicated treatments were added in 1% FBS containing media, for the indicated times. Finally, spheres were fixed with 4% formaldehyde and imaged using a ZEISS Axio Observer microscope. QuPath v0.3.2 software was used to quantify the area covered by cells at day 0 and at final time point pictures. Core growth was calculated as follows: increment area = area Tf/area T0. To measure invasive growth, the day 0 core detection was duplicated final time point picture and expanded at a 200μm distance. The pixel classifier was used to classify all cells as detections. Core and core +200μm annotation measurements of total area and area occupied by the classifier were exported to Excel. Invasion was calculated as follows: invasion = area occupied by cells/total area between core and core +200μm.

Where indicated, spheroids were stained for F-actin. Spheroids were permeabilised using 0.5% Triton X-100 in 5% BSA-PBS overnight, washed 5 min with PBS-T 0.01%, washed 3 × 5min with PBS, blocked in 5% BSA-PBS for 1hour and incubated with Alexa Fluor 546-phalloidin (A22283, Thermo Fisher, 1:400 in 0.3% Triton X-100-5% BSA-PBS) for 2 h at room temperature. Finally, spheroids were washed 5 min with PBS-T 0.01% and 3 × 5min with PBS. Images were taken with a Zeiss LSM 880 confocal microscope with Airyscan super resolution mode (Carl Zeiss, Germany). Zen software (https://www.zeiss.com/microscopy/us/products/software/zeiss-zen.html) was used to acquire images (Carl Zeiss, Germany).

Western blotting

Cells were lysed in Laemmli Lysis Buffer and snap frozen. Then, lysates were boiled for 5 min, sonicated for 15 seconds and spun down. Cell lysates were resolved by SDS-polyacrylamide gels (SDS-PAGE) in non-reducing conditions and transferred to PVDF filters (0.45μm, Immobilion). Membranes were blocked in 5% BSA in 0.1% Tween 20-TBS. Primary antibodies were incubated overnight at 4°C. ECL Plus or Prime ECL detection System (GE Healthcare) with HRP-conjugated secondary antibodies (Amersham ECL Rabbit IgG, HRP-linked whole Ab (from donkey) NA934 and Amersham ECL Mouse IgG, HRP-linked whole Ab (from sheep) NA931, 1:10 000 GE Healthcare) were used for detection. Bands were quantified using Fiji 1.53t software (http://fiji.sc).

Measurement of extracellular ROS

Extracellular ROS levels were assessed using the Amplex Red Hydrogen Peroxide/Peroxidase Assay Kit (Thermo Fisher Scientific) following the manufacturer's protocol. A375M2 scramble and A375M2 siSLC7A11 cells were incubated overnight in phenol red-free, serum-free DMEM. The next day, conditioned media were collected without centrifugation and immediately processed for H_2O_2

quantification. Samples were incubated with 50 μM Amplex Red reagent and 0.2 U/mL horseradish peroxidase (HRP) in a 96-well plate for 1 h at room temperature, protected from light. Absorbance was measured at 560 nm, and H_2O_2 levels were analyzed. Positive and negative controls for H_2O_2 were included to validate assay performance. Data were expressed as fold change in absorbance relative to control conditions.

Measurement of intracellular ROS

A375M2 cells were seeded in 6-well plates at approximately 250,000 cells per well. The following day, cells were treated with or without 10 mM GSH. One hour later, the cells received either DMSO or ROCK inhibitor treatment. After 24 h, cells were treated with trypsin, centrifuged, and resuspended in a solution containing 5 μM mitoSOX to assess mitochondrial ROS or 5 μM CM-H2DCFDA to measure total ROS. The cells were then incubated at 37°C for 30 min. Following staining, 500 μL of FACS buffer (1% BSA, 2 mM EDTA, and 0.1% NaN_3 in PBS) was added to each sample, which was immediately acquired using a Beckman Coulter CytoFLEX LX Cell Analyzer (for A375M2 scramble/siSLC7A11 cells and GSK269962A treatment) or BD FACS CANTO II flow cytometer (for H1152 treatment) and analyzed with FlowJo version 7.6.5 software (Tree Star).

Metabolite extraction and LC-MS analysis

A375M2 scramble and A375M2 siSLC7A11 cells were seeded at 250,000 cells per well in a 6-well plate and incubated for 48 h to reach ~70–80% confluence. 24 h prior to extraction, cells were treated with 250 μM L-BSO in 1% FBS, menadione in 1% FBS, or corresponding vehicle controls.

For the $^{13}C_2$,^{15}N -labelled GSH (Cambridge isotope, CNLM-6245) study, cells were supplemented with 10 mM ^{13}C-GSH in 1% FBS media overnight prior to extraction.

On the day of extraction, plates were placed on ice and 500μL media was collected. Cells were then washed twice with cold 30mM N-Ethylmaleimide (NEM: Sigma, E3876)-PBS (pH 7.4) and snap-frozen in liquid nitrogen then placed back on ice. Cell samples were collected using 100μL of pre-cooled (−20°C) extraction buffer (Methanol/Acetonitrile/Water, 2/2/1 v/v:v supplemented with 1mM NEM) using a cell-scraper and transferred into an Eppendorf tube. Media samples, and unused media serving as control, were mixed (1/1 v/v) with extraction buffer. Samples were then centrifuged for 10min at +4°C, 10.000rpm. Cell and media supernatant were then mixed with cold acetonitrile (1/1 v/v), centrifuged again and the supernatant transferred into LC/MS vials for analysis.

Metabolomic analysis was performed using a UHPLC-Q/TOF system. Chromatographic separation was carried out on an Agilent 1290 Infinity II Binary Pumpusing a InfinityLab Poroshell 120 EC-C18 column (2.7μm, 3.0 mm × 150 mm, - Agilent: 693975-302T) maintained at 40°C. Samples were maintained at 4°C in an autosampler and injection volume was set to 10μL. The elution of metabolites through the column was achieved at a flow rate of 0.200mL/min using solvent A, water containing 0.1% formic acid and solvent B, acetonitrile containing 0.1% formic acid, both supplemented with 2.5μM InfinityLab Deactivator Additive. The following gradient was used for elution: 0min, 1%B; 1.5min, 1%B; 15min, 80%B; 17min, 99%B; 19min, 99%B; 20min, 1%B. Mass spectrometry analysis was performed on an Agilent 6546 LC/Q-TOF mass spectrometer in positive polarity mode. Agilent Masshunter Workstation Data Acquisition software (https://www.agilent.com/en/product/software-informatics/mass-spectrometry-software/data-acquisition) was used for data acquisition. For data analysis, Agilent Profinder B.8.0.00 was used with a library of pre-determined retention times (+/− 0.20min shift) and accurate mass (+/− 15ppm shift) for metabolites of interests. Data was normalized to protein concentration, determined using the Pierce BCA Protein Assay Kit.

Analysis of gene expression from public databases

Normalized gene expression microarray data of rounded-amoeboid melanoma cells (GSE23764)[7] were analyzed by comparing rounded-amoeboid A375M2 cells to more elongated and less contractile A375P cells or to A375M2 cells treated with ROCK1/2 inhibitors (H1152 and Y27632) or blebbistatin. Heatmaps were performed using Morpheus (Broad Institute).

Gene expression data of invading cells compared to the non-migratory core from MV3 spheroids embedded in collagen I was used to analyze expression of SLC7A11 (GSE215750).[33]

Gene expression data from four melanocyte datasets GSE4570,[64] GSE4840,[65] and data from melanoma cell lines (Mannheim cohort GSE4843[65] and Philadelphia cohort GSE4841[65]) was used to analyze expression of SLC7A11. Gene expression data of human melanoma samples from published microarray studies was used to analyze expression of SLC7A11 in melanoma progression. From public database GEO (Gene Expression Omnibus) we extracted expression data from the Kabbarah: GSE46517[66]; Talantov: GSE3189[67]; and Riker: GSE7553[68] series. Data were normalized using Gene Pattern (http://www.broadinstitute.org/cancer/software/genepattern/).

Gene expression data of human melanoma samples from The Cancer Genome Atlas (TCGA) database (http://cancergenome.nih.gov/) was obtained from cBioportal (www.cbioportal.org) and used to analyze gene expression in melanoma progression.

For ferroptosis signature analysis, mRNA data for Skin Cutaneous Melanoma TCGA pan-cancer atlas project was obtained from cBioportal (www.cbioportal.org) in RSEM normalised expression. Only metastatic samples were used, and patients were separated in high and low SLC7A11 by median value, where only the high expression patients were selected for further analysis. SLC7A11 high patients were separated again by median value of RSEM mRNA expression into high or low GPX4 expression and fold change calculated as high versus low expression. Heatmap shows log2 fold change of each gene in the ferroptosis signature and statistical value was calculated using unpaired t test. Heatmap was generated using Morpheus (Broad Institute; https://software.broadinstitute.org/morpheus/).

Immunohistochemistry

Tumor tissues were formalin-fixed and paraffin-embedded as per standard protocols. Sections of 4μm thickness were heated at 60°C for 1 h and then incubated in xylene and ethanol series, with 2 × 5 min H_2O_2/ethanol incubations to block endogenous peroxidase. Antigen retrieval was performed in Antigen Unmasking Solution pH 6 (H-3300, Vector Labs) using a pressure cooker system (110°C for 10 min). Samples were washed in Dako Wash Buffer (S3006), before primary antibody incubation (overnight, 1:300 anti-SLC7A11, CST #12691 for human samples, #98051 for mouse samples), diluted in Antibody Diluent Reagent Solution (003218, invitrogen/ThermoFisher Scientific). Samples were washed and incubated with ImmPRESS polymer secondary goat anti-rabbit antibody (goat anti-rabbit, RTU, Vector Labs, MP-7451) for 45 min. The reaction was developed using VIP peroxidase substrate solution (Vector Labs, SK-4600) for 10 min. All incubations were carried out at room temperature. Slides were counterstained with haematoxylin and mounted using DPX mounting medium (06522-500 ML, sigma). Slides were imaged using the NanoZoomer S210 slide scanner (Hamamatsu, Japan).

Staining quantification was performed using QuPath 0.1.2.[69] Whole section images (WSI) from mouse tissue and TMAs were analyzed performing positive cell detection, and three different thresholds were applied according to the intensity scores (0, 1, 2 and 3). Next, the software was trained by creating a random tree classification algorithm combined with the intensity information, to differentiate tumor from stroma, necrosis and immune cells. Then, IHC staining was graded semi-quantitatively by considering the percentage and intensity of the staining. A histologic score (Hs) was obtained from each sample, and values ranged from 0 (no immunoreaction) to 300 (maximum immunoreactivity) arbitrary units. The score was obtained by applying the following formula, Hs = 1 × (% light staining) + 2 × (% moderate staining) + 3 × (% strong staining). Cell segmentation was performed using QuPath v0.5.1, leveraging the StarDist HE heavy augmentation pretrained model for H&E-like staining. The model was applied to SLC7A11-stained immunohistochemistry (IHC) images after manual annotation of tumor body (TB) and invasive front (IF) regions. Prior to segmentation, images were pre-processed with stain vector normalization to optimise compatibility with the pretrained model. The StarDist model outputs included precise nuclear and cell boundaries, which were used to extract morphological metrics.

QUANTIFICATION AND STATISTICAL ANALYSIS

Statistical analyses were performed using GraphPad Prism 10.1.1 software (GraphPad, San Diego). The following statistical analysis were used: one sample t test, unpaired t test, paired t test, Mann–Whitney’s test, one-way ANOVA with Tukey’s, or Dunnett’s post hoc test, and two-way ANOVA with Fisher’s LSD test. Data were represented in bar graphs and dot plots as mean ± standard error of the mean (SEM) and violin plots as median with interquartile range. In Figure legends, “n” means number of independent experiments unless otherwise stated. Significance was defined as $p < 0.05$, $^{*}p < 0.05$, $^{**}p < 0.01$, $^{***}p < 0.001$, $^{****}p < 0.0001$, ns not significant.